Design, analysis, and transmission system performance of a 41 GHz silicon photonic modulator

David Patel,[*] **Samir Ghosh, Mathieu Chagnon, Alireza Samani,**
Venkat Veerasubramanian, Mohamed Osman, and
David V. Plant

Photonic Systems Group, Department of Electrical and Computer Engineering,
McGill University, Montréal, Québec, H3A 0E9, Canada

[*]*david.patel@mail.mcgill.ca*

Abstract: The design and characterization of a slow-wave series push-pull traveling wave silicon photonic modulator is presented. At 2 V and 4 V reverse bias, the measured -3 dB electro-optic bandwidth of the modulator with an active length of 4 mm are 38 GHz and 41 GHz, respectively. Open eye diagrams are observed up to bitrates of 60 Gbps without any form of signal processing, and up to 70 Gbps with passive signal processing to compensate for the test equipment. With the use of multi-level amplitude modulation formats and digital-signal-processing, the modulator is shown to operate below a hard-decision forward error-correction threshold of 3.8×10^{-3} at bitrates up to 112 Gbps over 2 km of single mode optical fiber using PAM-4, and over 5 km of optical fiber with PAM-8. Energy consumed solely by the modulator is also estimated for different modulation cases.

OCIS codes: (130.3120) Integrated optics devices; (250.4110) Modulators; (230.7020) Traveling-Wave Devices; (200.4650) Optical interconnects.

References and links

1. D. Miller, "Device requirements for optical interconnects to silicon chips," Proc. IEEE **97**, 1166–1185 (2009).
2. A. Novack, M. Gould, Y. Yang, Z. Xuan, M. Streshinsky, Y. Liu, G. Capellini, A. E.-J. Lim, G.-Q. Lo, T. Baehr-Jones, and M. Hochberg, "Germanium photodetector with 60 GHz bandwidth using inductive gain peaking," Opt. Express **21**, 28387–28393 (2013).
3. R. Walker, "High-speed III-V semiconductor intensity modulators," IEEE J. Quantum Electron. **27**, 654–667 (1991).
4. R. Spickermann, S. Sakamoto, and N. Dagli, "In traveling wave modulators which velocity to match?" in "Lasers and Electro-Optics Society Annual Meeting, 1996. LEOS 96., IEEE," , vol. 2 (1996), vol. 2, pp. 97–98 vol.2.
5. N. Jaeger and Z. Lee, "Slow-wave electrode for use in compound semiconductor electrooptic modulators," IEEE J. Quantum Electron. **28**, 1778–1784 (1992).
6. J. Shin, S. Sakamoto, and N. Dagli, "Conductor loss of capacitively loaded slow wave electrodes for high-speed photonic devices," J. Lightw. Technol. **29**, 48–52 (2011).
7. S. Akiyama, H. Itoh, S. Sekiguchi, S. Hirose, T. Takeuchi, A. Kuramata, and T. Yamamoto, "InP-based Mach-Zehnder modulator with capacitively loaded traveling-wave electrodes," J. Lightw. Technol. **26**, 608–615 (2008).
8. Y. Cui and P. Berini, "Modeling and design of GaAs traveling-wave electrooptic modulators based on capacitively loaded coplanar strips," J. Lightw. Technol. **24**, 544–554 (2006).
9. G. Li, T. Mason, and P. Yu, "Analysis of segmented traveling-wave optical modulators," J. Lightw. Technol. **22**, 1789–1796 (2004).
10. P. Dong, L. Chen, and Y.-K. Chen, "High-speed low-voltage single-drive push-pull silicon Mach-Zehnder modulators," Opt. Express **20**, 6163–6169 (2012).

11. L. Chen, P. Dong, and Y.-K. Chen, "Chirp and dispersion tolerance of a single-drive push-pull silicon modulator at 28 Gb/s," IEEE Photon. Technol. Lett. **24**, 936–938 (2012).
12. M. Poulin, C. Latrasse, J.-F. Gagne, Y. Painchaud, M. Cyr, C. Paquet, M. Osman, S. Lessard, and D. V. Plant, "107 Gb/s PAM-4 transmission over 10 km using a SiP series push-pull modulator at 1310 nm," in "European Conference on Optical Communications (ECOC), Paper Mo.4.5.3" (2014).
13. M. Chagnon, M. Osman, M. Poulin, C. Latrasse, J.-F. Gagné, Y. Painchaud, C. Paquet, S. Lessard, and D. Plant, "Experimental study of 112 Gb/s short reach transmission employing PAM formats and SiP intensity modulator at 1.3 μm," Opt. Express **22**, 21018–21036 (2014).
14. R. Ding, Y. Liu, Y. Ma, Y. Yang, Q. Li, A. E.-J. Lim, G.-Q. Lo, K. Bergman, T. Baehr-Jones, and M. Hochberg, "High-speed silicon modulator with slow-wave electrodes and fully independent differential drive," J. Lightw. Technol. **32**, 2240–2247 (2014).
15. F. Merget, S. S. Azadeh, J. Mueller, B. Shen, M. P. Nezhad, J. Hauck, and J. Witzens, "Silicon photonics plasma-modulators with advanced transmission line design," Opt. Express **21**, 19593–19607 (2013).
16. C. DeRose, D. Trotter, W. Zortman, and M. Watts, "High speed travelling wave carrier depletion silicon Mach-Zehnder modulator," in "Optical Interconnects Conference, 2012 IEEE," (2012), pp. 135–136.
17. J. Witzens, T. Baehr-Jones, and M. Hochberg, "Design of transmission line driven slot waveguide Mach-Zehnder interferometers and application to analog optical links," Opt. Express **18**, 16902–16928 (2010).
18. J. Ding, H. Chen, L. Yang, L. Zhang, R. Ji, Y. Tian, W. Zhu, Y. Lu, P. Zhou, and R. Min, "Low-voltage, high-extinction-ratio, Mach-Zehnder silicon optical modulator for CMOS-compatible integration," Opt. Express **20**, 3209–3218 (2012).
19. H. Yu and W. Bogaerts, "An equivalent circuit model of the traveling wave electrode for carrier-depletion-based silicon optical modulators," J. Lightw. Technol. **30**, 1602–1609 (2012).
20. R. Ding, Y. Liu, Q. Li, Y. Yang, Y. Ma, K. Padmaraju, A. E.-J. Lim, G.-Q. Lo, K. Bergman, T. Baehr-Jones, and M. Hochberg, "Design and characterization of a 30-GHz bandwidth low-power silicon traveling-wave modulator," Opt. Commun. **321**, 124 – 133 (2014).
21. X. Zhang, B. Lee, C. yun Lin, A. Wang, A. Hosseini, and R. Chen, "Highly linear broadband optical modulator based on electro-optic polymer," Photonics Journal, IEEE **4**, 2214–2228 (2012).
22. Y. Yang, Q. Fang, M. Yu, X. Tu, R. Rusli, and G.-Q. Lo, "High-efficiency Si optical modulator using Cu travelling-wave electrode," Opt. Express **22**, 29978–29985 (2014).
23. H. Xu, X. Li, X. Xiao, P. Zhou, Z. Li, J. Yu, and Y. Yu, "High-speed silicon modulator with band equalization," Opt. Lett. **39**, 4839–4842 (2014).
24. D. Frickey, "Conversions between S, Z, Y, h, ABCD, and T parameters which are valid for complex source and load impedances," IEEE Trans. Microw. Theory Techn. **42**, 205–211 (1994).
25. L. Chrostowski and M. Hochberg, *Silicon Photonics Design* (Cambridge University, 2015).
26. A. Novack, Y. Liu, R. Ding, M. Gould, T. Baehr-Jones, Q. Li, Y. Yang, Y. Ma, Y. Zhang, K. Padmaraju *et al.*, "A 30 GHz silicon photonic platform," in "SPIE Optics+ Optoelectronics," (International Society for Optics and Photonics, 2013), pp. 878107–878107.
27. M. A. Guillen-Torres, M. Caverley, E. Cretu, N. A. Jaeger, and L. Chrostowski, "Large-area, high-Q SOI ring resonators," in "Photonics Conference (IPC), 2014 IEEE," (2014), pp. 336–337.
28. D. Patel, V. Veerasubramanian, S. Ghosh, A. Samani, Q. Zhong, and D. V. Plant, "High-speed compact silicon photonic Michelson interferometric modulator," Opt. Express **22**, 26788–26802 (2014).
29. S. Akiyama, M. Imai, T. Baba, T. Akagawa, N. Hirayama, Y. Noguchi, M. Seki, K. Koshino, M. Toyama, T. Horikawa, and T. Usuki, "Compact PIN-diode-based silicon modulator using side-wall-grating waveguide," IEEE J. Sel. Topics Quantum Electron. **19**, 74–84 (2013).
30. W. A. Ling, I. Lyubomirsky, and O. Solgaard, "Digital quadrature amplitude modulation with optimized non-rectangular constellations for 100 Gb/s transmission by a directly-modulated laser," Opt. Express **22**, 10844–10857 (2014).
31. T. Baehr-Jones, R. Ding, Y. Liu, A. Ayazi, T. Pinguet, N. C. Harris, M. Streshinsky, P. Lee, Y. Zhang, A. E.-J. Lim, T.-Y. Liow, S. H.-G. Teo, G.-Q. Lo, and M. Hochberg, "Ultralow drive voltage silicon traveling-wave modulator," Opt. Express **20**, 12014–12020 (2012).
32. M. Streshinsky, R. Ding, Y. Liu, A. Novack, Y. Yang, Y. Ma, X. Tu, E. K. S. Chee, A. E.-J. Lim, P. G.-Q. Lo, T. Baehr-Jones, and M. Hochberg, "Low power 50 Gb/s silicon traveling wave Mach-Zehnder modulator near 1300 nm," Opt. Express **21**, 30350–30357 (2013).
33. IEEE P802.3bs 400 GbE Task Force. http://www.ieee802.org/3/bs .
34. P. Dong, X. Liu, S. Chandrasekhar, L. Buhl, R. Aroca, and Y.-K. Chen, "Monolithic silicon photonic integrated circuits for compact 100$^+$ Gb/s coherent optical receivers and transmitters," Selected Topics in Quantum Electronics, IEEE Journal of **20**, 150–157 (2014).
35. Y. Vlasov, "Silicon CMOS-integrated nano-photonics for computer and data communications beyond 100G," IEEE Commun. Mag. **50**, s67–s72 (2012).
36. H. Subbaraman, X. Xu, A. Hosseini, X. Zhang, Y. Zhang, D. Kwong, and R. T. Chen, "Recent advances in silicon-based passive and active optical interconnects," Opt. Express **23**, 2487–2511 (2015).
37. H. T. Chen, "Development of an 80-Gbit/s InP-based Mach-Zehnder modulator," Ph. D. Dissertation, Dept. Elect.

1. Introduction

Silicon photonics (SiP) is of immense interest for short-reach optical interconnects because of its CMOS compatibility, high yield and accurate fabrication resulting in lower fabrication costs for high-volume production, and large index contrast allowing dense optical integration. In addition, optical interconnects are able to achieve high bitrate and energy efficient transmission over ware-house scale distances compared to their electrical counterpart [1]. Silicon modulators are an essential component of such SiP communication links and significant research is dedicated in developing devices with a large bandwidth and low drive-voltages. It is desirable to have modulators with very high bandwidths to reduce the number of multiplexed channels, which would otherwise require additional hardware and result in increased costs and energy consumption. Furthermore, 60 GHz photo-detectors [2] have been demonstrated in this technology, but bandwidths of modulators with 3-4 mm of modulating length have remained lower.

The carrier-depletion effect, onto which relies the electro-optical modulation in silicon is relatively weak and long phase shifting regions for low drive voltages are therefore necessary. This requires traveling wave modulator designs as opposed to shorter lumped modulators. In order to maximize the electro-optic (EO) bandwidth of a traveling wave Mach-Zehnder modulator (TWMZM), three main aspects need to be considered [3]: (1) the microwave attenuation should be as low as possible; (2) the microwave group velocity must match the optical group velocity; and (3) the impedance of the transmission line should be matched to the driver and termination impedance to reduce reflections that can contribute to inter-symbol-interference (ISI) and to obtain the highest possible voltage drop across the modulator. Throughout the paper, we discuss the design of a SiP TWMZM with respect to these three criteria.

The phase and group velocity of the microwave is determined by the geometry of the electrodes, the material system, and the loading of the p-n junction. With a series push-pull (SPP) modulator, the p-n junction loaded index of the transmission line is estimated to be lower than the optical group index resulting in the optical and microwave packets traveling through the modulator at different velocities. The mismatch results in a reduced efficiency at high modulation speeds and therefore lower bandwidths [4]. The TWMZM reported here uses electrodes formed with 'T'-shaped extensions to reduce the speed of the microwave signal and obtain a group velocity closer to that of the optical wave. At the same time, the microwave loss is reduced by using a series push-pull (SPP) structure. SPP modulators with slow-wave effect from capacitive loading have been studied extensively in III-V compound semiconductor technologies [3, 5–9]. However, silicon SPP modulators have been reported by only a few select groups [10–13]. Silicon TWMZMs with unloaded slow-wave electrodes have been published in [11, 14–16], of which only [11] and [16] are SPP. Due to the tremendous research on the topic of EO modulators, detailed electrode design and analysis have also been reported abundantly, particularly in compound semiconductor modulators [3, 5–9]. In silicon-on-insulator (SOI), notable transmission line modeling are described in [14, 17–20]. Although SPP TWMZMs with slow-wave electrodes have been demonstrated, their design, analysis, and detailed characterization have yet to be reported. and are presented in this paper. The design of silicon TWMZMs are highly dependent on the p-n junction resistance and capacitance and therefore also the bias voltages. This is not the case for $LiNbO_3$ or other modulators based on electro-optics effects and therefore transmission line design is simplified [21].

Section 2 describes the design of unloaded co-planar strip (CPS) electrodes, the use of 'T'-shaped extensions for an increase in microwave effective index, and the effect of the p-n junction loading on the CPS transmission line. In section 3, small signal characterization and modulation experiments with and without digital-signal-processing (DSP) are presented. Our

TWMZM has a measured -3 dB EO bandwidth of 38 GHz and 41 GHz at 2 V and 4 V reverse bias, respectively. To the best of our knowledge, this is the highest bandwidth reported to date in this fabrication technology for a modulator with electrodes that have 4 mm of p-n junction loading. The closest reported bandwidth of a modulator fabricated in an identical fabrication process is 27 GHz at 1 V reverse bias for a modulator that is 1 mm shorter [14]. Very recently, a bandwidth of 37 GHz at -5 V bias was reported with a 3 mm long modulator and a custom doping compensation process and copper electrodes [22]. As will be discussed, shorter modulators have lower microwave losses and thus inherently have higher bandwidths. For instance, a 55 GHz modulator with only 0.75 mm has been recently reported [23]. Despite having a higher bandwidth, short modulators in a process with a similar modulation efficiency will require larger drive voltages to obtain the same optical modulation amplitude. Longer modulators may have a low DC V_π, but can end up with high RF V_π due to lower bandwidths. Our modulator achieves a high bandwidth with a relatively long modulating length without using a doping compensation process.

In a back-to-back configuration, the modulator operates error-free up to 45 Gbps, the limit of our photoreceiver. Open eyes are visible up to 60 Gbps, and with passive analog pre-emphasis, up to 70 Gbps. Using DSP, error-free (defined as a bit-error-rate of 3.8×10^{-3} at 112 Gbps) transmission of 100 Gbps PAM-4 signals over 2 km of single mode fiber (SMF-28e+) and 100 Gbps PAM-8 signals over 5 km of SMF-28e+ is demonstrated. Energy consumed by the modulator for these different driving configurations are also calculated.

2. Device design and fabrication

2.1. Device structure and layout

The schematic of the TWMZM is shown in Fig. 1. The modulator was fabricated in a 220 nm SOI wafer with a 750 Ω-cm silicon substrate at IME A*STAR on an OpSIS multi-project wafer run. The diode-waveguide structures were formed by doping rib waveguides that are 500 nm wide and 220 nm high on a 90 nm slab for operation at 1550 nm. The modulator can, however, be re-designed for operation at 1310 nm with minute changes in the waveguide and electrode design. The electrodes were fabricated in the top 2-μm thick aluminum metal layer with the dimensions indicated in the sub-caption of Fig. 1.
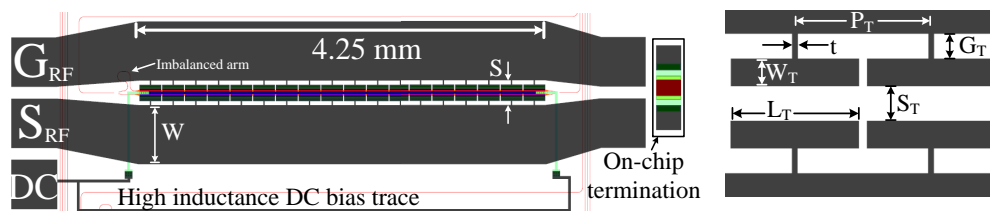

Fig. 1: Layout schematic of the SPP TWMZM and a magnified view of the 'T'-shaped extensions (schematic not to scale). The dimensions are: $W = 120 \ \mu m$, $S = 51 \ \mu m$, $t = 2 \ \mu m$, $S_T = 12.6 \ \mu m$, $G_T = 9.2 \ \mu m$, $W_T = 10 \ \mu m$, $L_T = 47 \ \mu m$, and $P_T = 50 \ \mu m$.

The p-n junction doping concentrations and positions were chosen to be identical to that reported in [14], thus allowing us to compare the performance of the modulators solely due to different electrode design and modulator structure. The modulator used three doping levels, and the cross-section of the fabricated SPP modulator is shown in Fig. 2. The intermediate doping levels (p+ and n+) provides a balance between optical loss, the p-n junction intrinsic bandwidth, and the microwave loss.

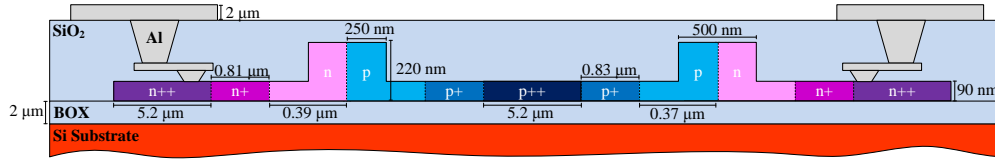The interferometer was formed using low-loss compact Y-branches as the input and output

Fig. 2: Cross-section schematic of the SPP TWMZM design on an SOI wafer (drawing not to scale).

couplers of the modulator. An intentional imbalance of 100 μm was incorporated to allow phase shift measurements and modulator biasing by tuning the wavelength. The modulator electrodes, from pad center to pad center, are 4.7-mm long and the net p-n junction loading is 4-mm.

The SPP configuration was formed by connecting the p-n junctions back to back as depicted by the cross-section in Fig. 2. The primary motivation for investigating a SPP structure is the reduction in microwave loss as detailed in section 2.4. The reduction in the capacitance, resulting from the two p-n junctions being in series, increases the velocity of the microwave, thus increasing the group velocity mismatch between the optical and electrical waves. This effect is compensated by using electrodes with 'T'-shaped extensions that have a high inductance and capacitance as will be described in section 2.3.

In a SPP structure, the biasing is done through an on-chip metal trace having a high-inductance instead of external bias-tees and this also allows for denser integration. A high-inductance trace is necessary to prevent the lower frequency components of the RF signal from being shorted to ground, which can potentially increase jitter, degrade SNR, and lead to baseline wander. In our design, the bias is applied via a high-inductance on-chip 6-mm long and 5-μm narrow metal. Reverse bias operation is ensured when $|V_{Bias}| \geq |V_{pp}/4|$, where V_{pp} is the driving voltage.

On the other hand, dual-drive modulators would require broadband microwave biasing circuit for each arm of the modulator. This complicates design and requires more area. Furthermore, dual-drive modulators also need to ensure each arm of the modulator is isolated to prevent cross-talk or use an unconventional driving scheme [15]. Alternatively, SPP modulators require only one single-ended driver as opposed to a differential or two single-ended drivers for dual-drive designs. The two drive signals required by dual-drive modulators reduces bandwidth density and depending on the method of integration will also increase connectorization costs. SPP designs, however, require higher driving voltage from a single driver and thus consume more dynamic power as discussed in section 3.8. It is to be noted that net voltages required are nearly the same for both types of modulators to obtain a similar optical modulation amplitude. Hence, the choice of which structure to use should be dictated by the application of the TWMZM.

The on-chip termination (OCT) is a 35-μm long and 50-μm wide n++ doped semiconductor having a 50 Ω resistance. As opposed to single or dual-drive modulators, the bias voltage of the SPP structure does not drop across the transmission line or the termination impedance. Hence, the RMS voltage across the OCT in a SPP modulator is smaller compared to a single or dual-drive modulator and therefore, the OCT's resistance is less affected by the nonlinearity shown in section 3.3.

2.2. Unloaded coplanar strip transmission line design

Analysis of unloaded CPS transmission lines were first performed to gauge the effect of introducing a slow-wave structure that utilizes 'T'-shaped extensions to the electrodes. Unloaded CPS transmission line simulations show that: a) a high microwave index is not possible; b) wider CPS transmission lines have little effect on reducing attenuation; and c) 10 μm or

larger spacing should be used. Furthermore, as will be shown in section 2.3, the characteristic impedance of the slow-wave electrodes can be approximated by the average of the impedance of two different simple CPS lines.

The two transmission line parameters that were varied are the width of the signal and ground electrodes, and the spacing between them, where only symmetric CPS transmission lines using the top 2-μm thick metal layer were studied. The simulation results of varying the electrode width and spacing at 30 GHz, obtained from a 3-D full-wave electromagnetic solver, are shown in Fig. 3.
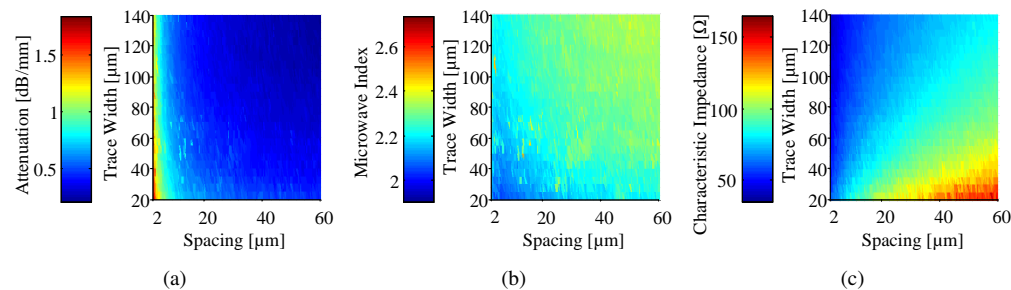
Fig. 3: Finite element method (FEM) simulations of unloaded symmetric CPS transmission lines at 30 GHz for different top-metal trace widths and spacing for (a) microwave attenuation, (b) effective phase index, and (c) characteristic impedance.

The microwave attenuation of an unloaded CPS, shown in Fig. 3(a), remains mainly below 0.75 dB/mm and increases for spacing smaller than approximately 20 μm. From additional FEM simulations using ANSYS HFSS, the loss in the conductor at 30 GHz was observed to be at least two orders of magnitude higher than the loss in the 750 Ω-cm silicon substrate. Beyond a spacing of approximately 20 μm, only a small reduction in attenuation is obtained with wider traces and/or larger spacing. This is due to the conductor loss at 30 GHz being dominated by the skin effect and therefore, only a small percentage of the cross-section is effective in reducing the resistive losses. In our design, a spacing of 12.6 μm was used between the 'T'-shaped segments (S_T) in order to minimize loss. Larger spacing would ensure a lower unloaded loss, but this would also require larger trace widths to obtain the same characteristic impedance as depicted by the simulation of Fig. 3(c). In addition, using a larger spacing would require a larger width of the common dopant (p++ of Fig. 2), which increases microwave loss as will be illustrated by the derivations in section 2.4. The conductor loss, which is arises from the skin effect, can be lowered by using a metal with higher conductivity such as copper. However, as shown in Section 2.4, the conductor loss is only a small portion of the total loss of a p-n junction loaded transmission line.

Figure 3(b) shows that the microwave index remains in the range of 2.1-2.4. The microwave index generally increases with increasing spacing and trace widths. As will be shown in section 2.3, the index can be increased to 2.7 using a slow-wave structure.

2.3. *Unloaded slow-wave transmission line*

Simulations of three cases illustrated in Fig. 4 were performed, where we define a slow-wave transmission line to include 'T'-shaped extensions as shown in Fig. 4(b). The simulated S-parameters from HFSS were converted to ABCD parameters using the formulation summarized in [24] to derive the attenuation, effective index, and characteristic impedance plotted in Fig. 5.

Figure 5(a) shows that the slow-wave CPS transmission line attenuation is similar to a transmission line with a small spacing (case (c)), and both have a larger attenuation than the trans-
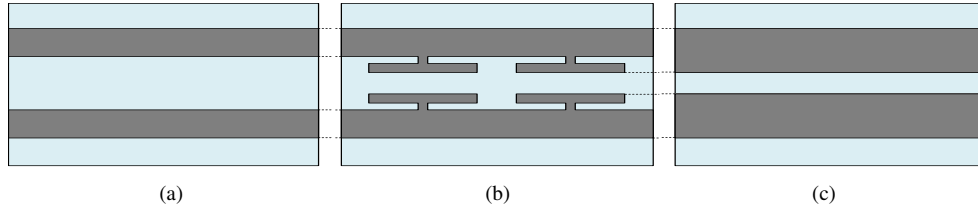
Fig. 4: Three simulation cases used to represent the effect of 'T'-shaped extensions on SOI CPS transmission lines. Case (a) represents a CPS transmission line without the 'T'-shaped extensions such that $W = 120\ \mu m$ and $S = 51\ \mu m$, case (b) is the slow-wave transmission line with dimensions indicated in Fig. 1, and case (c) is a wider CPS transmission line and a smaller spacing such that $W = 139.2\ \mu m$ and $S = 12.6\ \mu m$.

mission line with a large spacing. This result shows that the attenuation is mainly determined by the spacing between the 'T'-shaped extensions S_T and that it is advantageous to use a slightly larger spacing between the 'T'-shaped extensions for lower loss as inferred by Fig. 3(a).
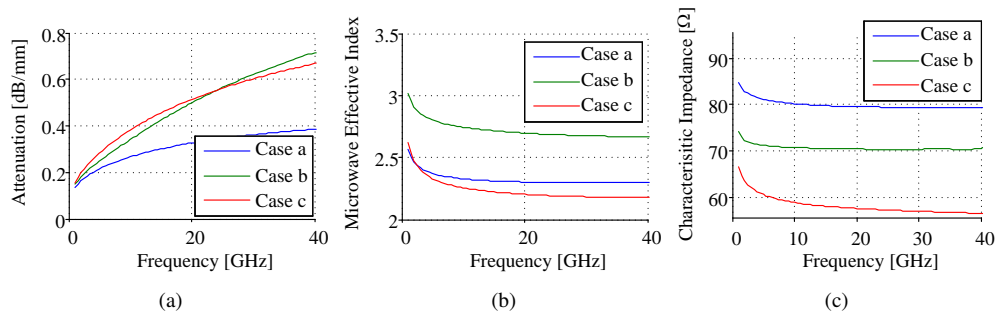

Fig. 5: Simulated (a) microwave attenuation, (b) microwave index, and (c) characteristic impedance of CPS transmission lines shown in Fig. 4.

Figure 5(b) illustrates that the slow-wave CPS transmission line has a higher index than the other two cases and that an effective index of 2.7 is obtained with this geometry at 30 GHz, a value that cannot be reached using simple CPS lines over a large range of trace widths and spacing as confirmed by Fig. 3(b). The effective index is also nearly constant above ∼10 GHz indicating that dispersion for the unloaded transmission lines is stronger at lower frequencies than at higher frequencies. The simulation also indicates that using 'T'-shaped extensions do not introduce additional dispersion which can lead to pulse distortion and ISI. For the purposes of velocity matching we use the effective index because of the low dispersion property. Design is further simplified because the index and impedance are constant in the high frequency regime; our modulator was designed using values at 30 GHz.

Figure 5(c) shows that the characteristic impedance of the slow-wave transmission line is approximately the average of the characteristic impedance of the other two cases: a CPS with a width of W and a spacing of S, and a CPS with a width of $W + G_T + W_T$ and a spacing of S_T. The impedance values for these two cases can be obtained from the simulations shown in Fig. 3(c). We chose 70 Ω for the characteristic impedance of the unloaded slow-wave transmission line based on the procedure that will be discussed in section 2.5.

Additional insight on the slow-wave effects in SOI CPS transmission lines can be obtained by mapping the simulated S-parameters to the telegrapher's RLGC model. The RLGC model will also later allow us to incorporate the effect of the p-n junction and perform S-parameter simu-
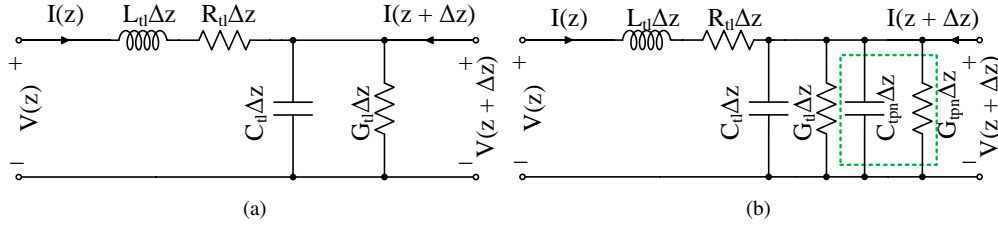
Fig. 6: Telegrapher's model of (a) an unloaded transmission line, and (b) of a transmission line loaded with a p-n junction. In this model, R_{tl} is resistance of the transmission line, L_{tl} is the inductance, C_{tl} is the capacitance, and G_{tl} is the leakage conductance between the two electrodes. All values are per unit length, and Δz represents a length of the transmission line that is much smaller than the effective wavelength λ_{eff} of the propagating wave ($\Delta z \ll \lambda_{eff}$). In (b) R_{tpn} and C_{tpn}, outlined in green, are the parallel equivalent of the series p-n junction resistance and capacitance.

lations in section 2.6. This model applies under the assumption of transverse electro-magnetic (TEM) or quasi-TEM wave propagation at all frequencies of interest, an assumption that was verified in [19]. The RLGC circuit model of an unloaded CPS transmission line is shown in Fig. 6(a). It should be noted that the RLGC parameters are frequency dependent with the inductance and capacitance typically becoming constant at high frequencies.

Using this model, the unloaded characteristic impedance Z_{0ul} and the propagation constant γ_{ul} are shown in Eq. (1) and Eq. (2), respectively, for the lossy and lossless ($\alpha = 0$, $R = 0$, and $G = 0$) case. Under the lossless assumption, the unloaded microwave index $n_{\mu,ul}$ can be represented by Eq. (3), where c_0 is the speed of light in vacuum. Equation (3) shows that a higher index can be obtained from higher inductance and capacitance. However, if the ratio of the inductance and capacitance is not maintained, then the characteristic impedance will also be affected.

$$Z_{0ul} = \sqrt{\frac{R_{tl} + j\omega L_{tl}}{G_{tl} + j\omega C_{tl}}} \overset{\text{lossless}}{=} \sqrt{\frac{L_{tl}}{C_{tl}}} \tag{1}$$

$$\gamma_{ul} = \alpha_{ul} + j\beta_{ul} = \sqrt{(R_{tl} + j\omega L_{tl})(G_{tl} + j\omega C_{tl})} \overset{\text{lossless}}{=} \underbrace{j\,\omega\sqrt{L_{tl}C_{tl}}}_{\beta_{ul}} \tag{2}$$

$$n_{\mu,ul} = \frac{c_0}{v_{\mu,ul}} = c_0\sqrt{L_{tl}C_{tl}} = c_0 C_{tl} Z_{0ul} = c_0 \frac{L_{tl}}{Z_{0ul}} \tag{3}$$

Under low-loss conditions and at very high frequencies, the following inequalities are satisfied: (1) $R_{tl} \ll \omega L_{tl}$, (2) $G_{tl} \ll \omega C_{tl}$, and (3) $R_{tl}G_{tl} \ll \omega^2 L_{tl}C_{tl}$. With these conditions, the expression for the characteristic impedance and the the microwave index approach the lossless case (Eq. (1) and Eq. (3), respectively). The unloaded low-loss propagation constant with the attenuation factor α_{ul} and phase constant β_{ul} then becomes:

$$\gamma_{ul} = \overbrace{\frac{1}{2}\left(\underbrace{\frac{R_{tl}}{Z_{0ul}}}_{\substack{\text{conductor}\\\text{loss}}} + \underbrace{G_{tl}Z_{0ul}}_{\substack{\text{dielectric}\\\text{loss}}} \right)}^{\alpha_{ul}\,[Np/m]} + j\,\overbrace{\omega\sqrt{L_{tl}C_{tl}}}^{\beta_{ul}\,[rad/m]} \tag{4}$$

The RLGC parameters extracted from the S-parameter simulations of the structures shown in Fig. 4 are plotted in Fig. 7. These simulation results indicate that the slow-wave CPS transmission line has the inductance of the narrow CPS transmission line illustrated in Fig. 4(a), but

at the same time, it has the capacitance of the CPS transmission line with the smaller spacing shown in Fig. 4(c)). From Eq. (3), this contributes to a higher microwave index leading to a slower propagating microwave. The inductance of the slow-wave CPS electrode is also dependent on the thickness of the stem denoted by t in Fig. 1. From additional simulations, it was observed that the inductance of the slow-wave CPS increased to that of the narrower CPS (case a) as the value of t decreased. For this reason, in our design t was chosen to be 2 μm, the smallest allowed by the fabrication design rules.
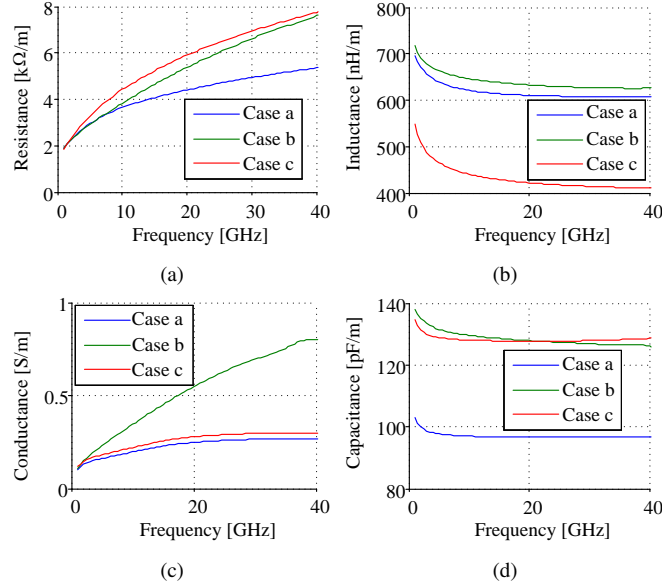

Fig. 7: Simulated per unit length (a) resistance (b) inductance (c) conductance, and (d) capacitance of CPS transmission lines.

A higher inductance, and thus a larger slowing factor, can be obtained by using a smaller width W and/or by increasing the distance G_T. This larger inductance would also increase the characteristic impedance, as described by Eq. (1), and this would need to be compensated by increasing the capacitance.

The extracted conductance of the slow-wave transmission line is much higher than the other two cases as shown in Fig. 7(c). However, the resistance of Fig. 7(a) and the attenuation of Fig. 5(a) have the same trend, thus indicating that the attenuation is dominated by the resistive losses rather than the conductance. Moreover, the resistance, like the attenuation, also varies with $\sqrt{f}$ as expected from the skin effect.

As opposed to other technologies, the junction capacitance is lateral in this SiP process. Hence, the capacitive loading due to the p-n junction does not increase significantly with the area of the pad ($W_T \times L_T$). Therefore, W_T was chosen to be 10 μm as required by the design rules for the metal and via stack underneath the pad. The choice of the length L_T is discussed in section 2.5.

2.4. p-n junction loaded transmission line design

Under reverse-bias operation, the p-n junction can be approximated by a series combination of the resistance R_{pn} from the contact to the edge of the depletion region and the depletion capacitance C_{pn}. The presence of the reverse biased p-n junction can be incorporated in to the RLGC model by transforming the series $R_{pn}C_{pn}$ elements into a parallel combination, denoted

by R_{tpn} and C_{tpn}, as shown in Fig. 6(b) [17]. It is assumed the insertion of the p-n junction does not introduce additional inductance and this is valid as long as little current flows through the silicon in the direction of wave propagation as indicated in [17]. For a SPP modulator, the model is simplified by merging the resistance and capacitance of the two diodes into one series RC model.

The depletion capacitance decreases with increasing reverse bias voltage, hence the characteristics of the loaded transmission line also become dependent on the bias voltage. The modulator design can only be optimized for one low-voltage bias point or for very high bias voltages (where RC values no longer change). The optimum bias point depends on the type of modulation performed with the modulator as will be experimentally shown in sections 3.5 to 3.7.3. However, our design was developed prior to this information and the value of the junction capacitance for a bias voltage of 0 V was used.

The loaded characteristic impedance Z_{0l} and propagation constant γ_l with the RLGC model are:

$$Z_{0l} = \sqrt{\frac{R_{tl} + j\omega L_{tl}}{(G_{tl} + R_{tpn}^{-1}) + j\omega(C_{tl} + C_{tpn})}} \tag{5}$$

$$\gamma_l = \alpha_l + j\beta_l = \sqrt{(R_{tl} + j\omega L_{tl})\left([G_{tl} + R_{tpn}^{-1}] + j\omega[C_{tl} + C_{tpn}]\right)} \tag{6}$$

By further applying the low-loss approximation, Eq. (5), Eq. (6), and the phase index $n_{\mu,l}$ can be expressed as:

$$Z_{0l} = \sqrt{\frac{L_{tl}}{C_{tl} + C_{tpn}}} \tag{7}$$

$$\gamma_l = \frac{1}{2}\left(\overbrace{\underbrace{\frac{R_{tl}}{Z_{0l}}}_{\substack{\text{conductor} \\ \text{loss}}} + \underbrace{\left(G_{tl} + R_{tpn}^{-1}\right)Z_{0l}}_{\substack{\text{dielectric} \\ \text{loss}}}}^{\alpha_l\,[Np/m]} \right) + j\,\overbrace{\omega\sqrt{L_{tl}\left(C_{tl} + C_{tpn}\right)}}^{\beta_l\,[rad/m]} \tag{8}$$

$$n_{\mu,l} = c_0\sqrt{L_{tl}\left(C_{tl} + C_{tpn}\right)} \tag{9}$$

From Eq. (6), insertion of the p-n junction adds R_{tpn} to α_l. Using the assumption that $\omega \ll \omega_{pn}$ ($\omega_{pn} = 1/R_{pn}C_{pn}$) to simplify the expression for the conductor and dielectric losses, the transformed junction resistance and capacitance can be approximated as $R_{tpn} \approx 1/\omega^2 C_{pn}^2 R_{pn}$ and $C_{tpn} \approx C_{pn}$. Including low-loss conditions, p-n junction loading effects on the Z_{ol} and $n_{\mu,l}$ can be summarized by Eq. (7) and Eq. (9) indicating that loading (via C_{pn}) reduces Z_{0l} and increases the $n_{\mu,l}$. Moreover, both conductor and dielectric losses are affected by the new loaded Z_{0l}. The loaded transmission line conductor loss α_{cl}, in terms of the DC (R_{DC}) and AC (R_{AC}) resistance, and the silicon dielectric loss α_{Sil} can be expanded to:

$$\alpha_{cl} = \frac{1}{2}\left(R_{DC} + R_{AC}\sqrt{f}\right)\sqrt{\frac{C_{tl} + C_{pn}}{L_{tl}}} \tag{10}$$

$$\alpha_{Sil} = \frac{1}{2}\left(4\pi^2 f^2 C_{pn}^2 R_{pn}\right)\sqrt{\frac{L_{tl}}{C_{tl} + C_{pn}}} \tag{11}$$

From Eq. (10), the conductor loss increases with $\sqrt{f}$; the silicon dielectric loss due to the p-n junction, Eq. (11), increases quadratically with f and C_{pn}, while increasing linearly with

R_{pn}. Therefore, the SPP configuration, which places two diodes in series ideally halving the capacitance and doubling the resistance, can reduce the silicon dielectric loss by 50% (if Z_{0l} is maintained).

From Eq. (8), lowering Z_{0l} increases the conductor loss and decreases the dielectric loss. Because dielectric losses are dominant, designing for a lower Z_{0l} will reduce microwave losses, as was done in [20]. In contrast to [20], where an impedance near 33-37 Ω was targeted, we designed our TWMZM for 50 Ω for a relatively larger power transfer (and also a larger modulating voltage along the transmission line) when driven by standard 50 Ω microwave drivers.

The total microwave loss obtained from HFSS simulations is plotted in Fig. 8(a). This simulation numerically confirms the trends in loss predicted by the derived equations. As per Eq. (11), a single p-n junction configuration has higher loss than two p-n junctions in series, particularly at higher frequencies, and the loss is significantly lower for the unloaded transmission line. Figure 8(a) also confirms that the loss due to the p-n junction is dominant since it follows the quadratic frequency dependency of Eq. (11) rather than the square-root dependency of Eq. (10). It should be noted that the electrode structures for all simulated cases were identical and that only the number of p-n junctions were changed. This implies that the single p-n junction case has a lower characteristic impedance, and thus lower loss than if the characteristic impedance was the same as the SPP case.
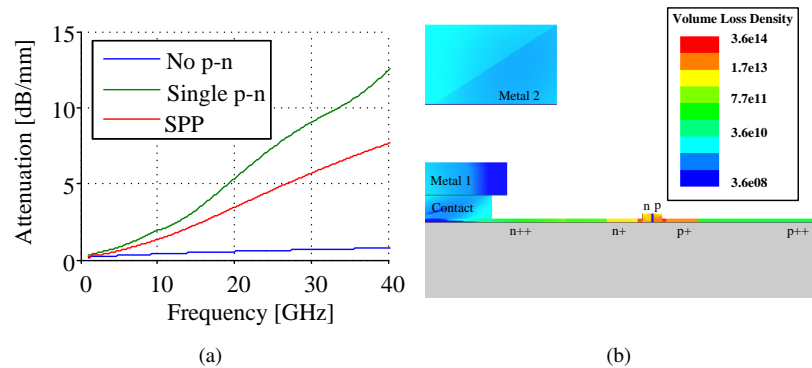

Fig. 8: (a) FEM simulations of microwave loss for cases of a transmission line without a p-n junction, a single p-n junction, and two p-n junction in series (for SPP). (b) Volume density loss for a TWMZM with a silicon p-n junction (logarithmic scale).

Figure 8(b) shows the volume loss density considering the metals, vias, and silicon layers. We note that the loss in the silicon is highest in the low doped 90 nm N and P regions, thus the numerical simulations are consistent with Eq. (11). Lower microwave loss can be obtained by bringing the highly doped region closer to the waveguide center, but this would increase the optical loss. In addition, the advanced dopants (n++ and p++) have a loss density that is about two orders of magnitude higher than that of the metal, thus it is not preferable to use a spacing (S_T) larger than necessary.

2.5. Simultaneous matching of impedance and velocity

The capacitive loading effect of the p-n junction can be reduced by using a segmented junction design instead of a continuous p-n junction along the entire length of the modulator. The amount of segmentation is defined by a fill factor k, which determines how much of a period is filled with the p-n junction.

Under low-loss conditions and high frequencies, the required unloaded characteristic impedance can be calculated in terms of the unloaded microwave index, and the targeted index

and impedance of the loaded line as [3,9]:

$$Z_{0ul} = \frac{n_{og}Z_{0l}}{n_{\mu,ul}} \qquad (12)$$

In the last equation, the targeted effective index of the loaded CPS line is made equal to the group index of the optical mode n_{og} for velocity matching ($n_{\mu,l} = n_{og}$). Additionally, the desired capacitance loading $C_{pn,d}$, here assumed solely due to the p-n junction, for simultaneous impedance and velocity matching is:

$$C_{pn,d} = \frac{n_{og}^2 - n_{\mu,ul}^2}{c_0 Z_{0l} n_{og}} \qquad (13)$$

The fill factor k can be determined from the actual junction capacitance $C_{pn,a}$ and the desired capacitance as: $k = C_{pn,d}/C_{pn,a}$.

The simulated group index of the rib waveguide is 3.89 near 1550 nm [25] and the simulated effective index of our electrode design, presented in section 2.3, is 2.7. Using these values in Eq. (12), the required unloaded impedance to achieve a loaded impedance of 50 Ω is 72 Ω. Because the characteristic impedance and the microwave effective index are related, our design geometry was obtained by solving for these two quantities iteratively from HFSS simulations. The simulated characteristic impedance of our design was 70 Ω, as discussed in section 2.3.

The required capacitance loading is estimated to 134.5 pF/m from Eq. (13). Using the measured junction capacitance of 230 pF/m at 0 V bias from [20], the fill factor requirement is 0.58. For a SPP modulator, the junction capacitance ideally halves and the fill factor increases to 1.17. A fill factor greater than unity is unrealistic and it signifies that the junction capacitance loading is insufficient to slow down the microwave. Therefore, slow-wave electrode structures using floating metal lines or with 'T'-shaped extensions can help. Although, the slow-wave factor was insufficient in our design for perfect matching of velocity and impedance, a larger slowing factor can be obtained with the design choices explained in section 2.3.

In our design, the p-n junction was segmented to reduce the current flowing longitudinally in the silicon based on the explanation in [20], but according to the simulations in [17], this should not be necessary. In addition, a small segmentation period should be chosen for simulations with lumped elements (RLGC model) and to ensure that the Bragg cut-off frequency ($f_{Bragg} \approx c_0/n_{\mu,l}\pi P_T$) [37] is beyond the desired bandwidth. Thus, a period P_T of 50 μm was used in this design. A gap of 3 μm was used between the 'T' segments, resulting in a L_T value of 47 μm and a fill factor of 94%.

2.6. Electro-optic simulation

The EE S_{21} simulation of the loaded transmission line was performed using the frequency-dependent RLGC values obtained from the FEM simulations presented in section 2.3 and the circuit model shown in Fig. 6(b). The simulated response did not match the measured responses of section 3.4 using previously published values of the p-n junction resistance and capacitance. This is due to variations in these values and will be further explained in section 3.1. A good agreement between the simulation and measured responses, as shown in Fig. 9(a), is obtained when the p-n junction resistance and capacitance are used as frequency-independent adjustable parameters.

Using the electrical simulations of Fig. 9(a), the EO response was simulated with minor modifications to the model developed in [9] and without using any additional fitting parameters. The simulated EO responses are shown in Fig. 9(b) and a -3 dB bandwidth greater than 45 GHz was expected at 4 V reverse bias. The bumps in the measured responses could not be replicated in the simulations. The presence of these bumps can impact the crossing of the -3 dB line by a
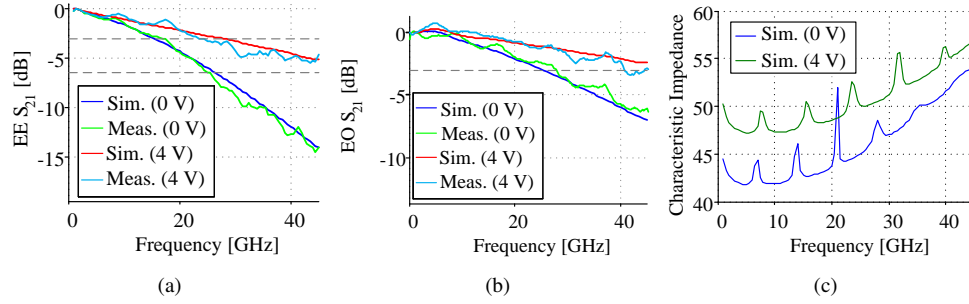
Fig. 9: Comparison of measured and simulated (a) EE S_{21} response with R_{pn} and C_{pn} as fitting parameters (dashed lines mark -3 dB and -6.4 dB), and (b) EO S_{21} response using the electrical simulation of (a) (dashed line marks -3 dB). Simulated characteristic impedance is shown in (c).

few GHz. In Fig. 9(c), the simulated characteristic impedance is plotted for 0 V and 4 V reverse bias. We observe that the impedance increases with frequency and also with higher reverse bias voltage. These trends are consistent with the impedance extracted from measurements shown in section 3.4.

3. Experiment and results

3.1. DC and optical characterization

In a push-pull modulator, it is desired to have equivalent phase shifts in both arms of the modulator, particularly to eliminate chirp. Furthermore, in a SPP modulator, the assumption that the capacitance is halved and that the resistance is approximately doubled, which is needed in the design process, relies on the diodes being equal. A different phase shift obtained from the two diodes under the same applied voltage is indicative of non-identical junction capacitance and resistance. The DC electro-optic measurements of this section attest that in reality the two diodes are not equivalent. This occurs due to the misalignment of dopant masks during fabrication. The effect of this alignment error can be reduced by placing diodes such that they have the same orientation, however, this is not possible to do in a SPP configuration since the diodes must be placed back-to-back.
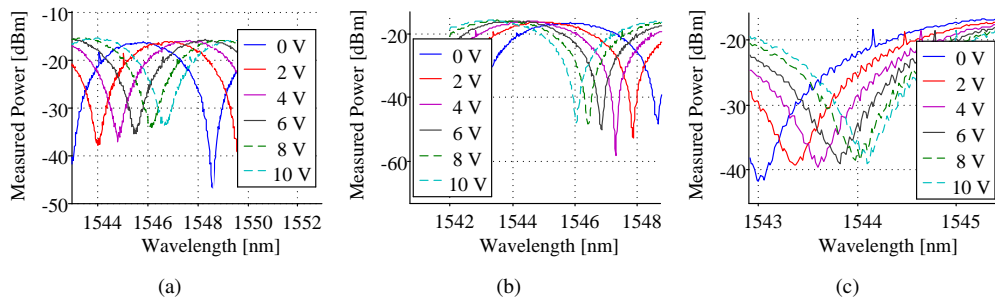

Fig. 10: Measured transmission spectra for (a) diode 1, (b) diode 2, and (c) both diodes under the same reverse bias voltage.

The measured transmission spectra of diode 1, diode 2, and then with both diodes under the same reverse bias voltage are shown in Fig. 10. From these transmission spectra, the insertion loss and the modulation phase shift were determined. At 0 V bias, the maximum output of the

modulator is -15 dBm. From a pair of grating couplers, the fiber-to-fiber I/O coupling loss was measured to be 8.4 dB. The routing loss from the grating couplers to the modulator I/O is calculated to be 2.8 dB (using the average strip waveguide loss of 2.4 dB/cm reported in [26]). Removing these contributions from the measured transmission spectra, the on-chip insertion loss of the modulator is a relatively low 3.8 dB. The routing loss, which is found to be comparable to the insertion loss of the modulator itself, can be reduced by using single-mode rib waveguides or low-loss multi-mode rib waveguides [27].

The corresponding phase shifts of each arm of the modulator are plotted as diode 1 and diode 2 in Fig. 11(a), and for both diodes under the same reverse bias in Fig. 11(b). Diode 1 attains a π phase shift at 7 V indicating a $V_\pi L$ of 2.8 V-cm. Diode 2 does not achieve a π phase shift up to a bias voltage of 10 V. Figure 11(b) quantifies the asymmetry in the modulation performance of the two arms of the MZM. Ideally, no phase shift should be visible in this test case, but due to mask alignment errors, significant deviation is observed.
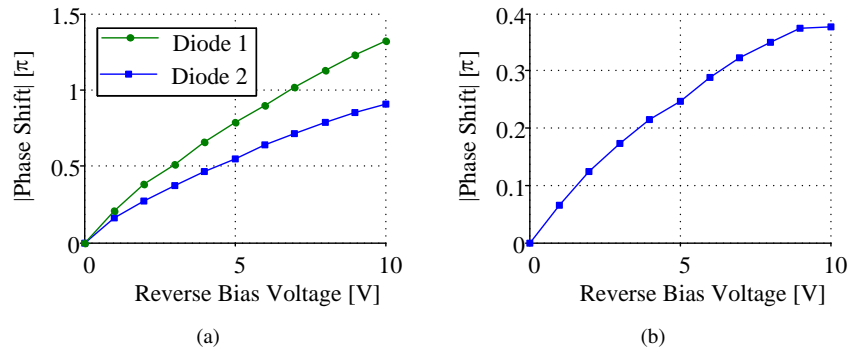

Fig. 11: Phase shift calculated from transmission spectrum for (a) diode 1 and diode 2, and (b) both diodes under the same reverse bias voltage.

3.2. p-n junction

The small signal parameters for the p-n junction were extracted by fitting the simulated S_{11} phase and magnitude of a series $R_{pn}C_{pn}$ circuit to the measured S_{11} parameter of a separate phase shifter (single p-n junction) with an identical structure to the ones used in the modulator. The extracted R_{pn}, C_{pn}, and the corresponding intrinsic bandwidth for different reverse bias voltages is plotted in Fig. 12. Intrinsic bandwidths greater than 100 GHz are observed, indicating that the junction response does not limit the bandwidth of the TWMZM. Based on the measurements presented in section 3.1, deviations from the plotted values are to be expected, and therefore these can only be used to approximate the design of TWMZMs. The measurements further show that the resistivity changes little for reverse bias voltages above 2 V bias and the changes in capacitance are small for reverse bias greater than 4 V. This is also reflected by the S-parameter responses of the TWMZM varying negligibly beyond 4 V bias.
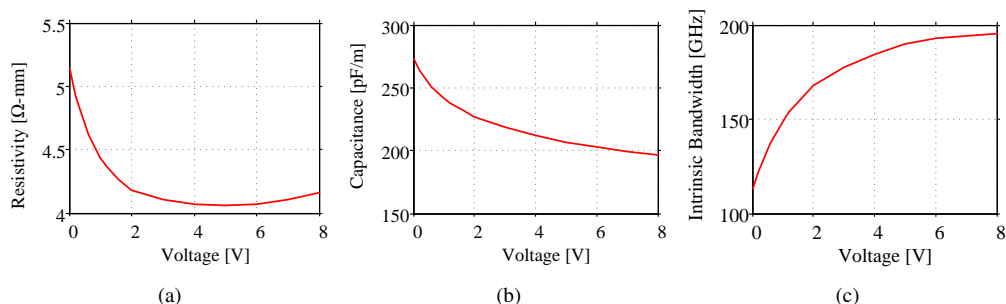
Fig. 12: Extracted p-n junction (a) resistivity, (b) capacitance, and (c) the associated intrinsic bandwidth for different reverse bias voltages.

3.3. On-chip termination

On-chip terminations (OCT) can be convenient for larger scale integration of MZMs by avoiding microwave connectorization or chip resistor bonding. Furthermore, with OCTs, custom impedance can be designed which can be used to perform equalization at the expense of modulation efficiency [19]. Although OCTs have been previously used in this technology, their DC and RF performance have not been reported in detail.

The measured results of an OCT designed to 50 Ω are shown in Fig. 13. From the I-V measurements of Fig. 13(a), the carrier velocity begins to saturate at about 3 V. The current saturation onset can be pushed to higher voltages by using a longer and wider OCT. The corresponding resistance is plotted in Fig 13(b) and it depicts that improper matching could result with very high RMS drive voltages, or with high reverse bias voltages in single or dual-drive modulators. The linearity of the resistance of the on-chip termination can be improved by using a wider and longer resistor. This will push the saturation current to higher voltages. Although silicon resistors are convenient, the mobility of silicon and thus the resistance also varies with temperature. An alternative is to use resistors made of thin metals, however, this would require additional masks and fabrication steps. In section 3.4, we also report the S-parameter measurements with and without the OCT, and nearly identical responses are observed.
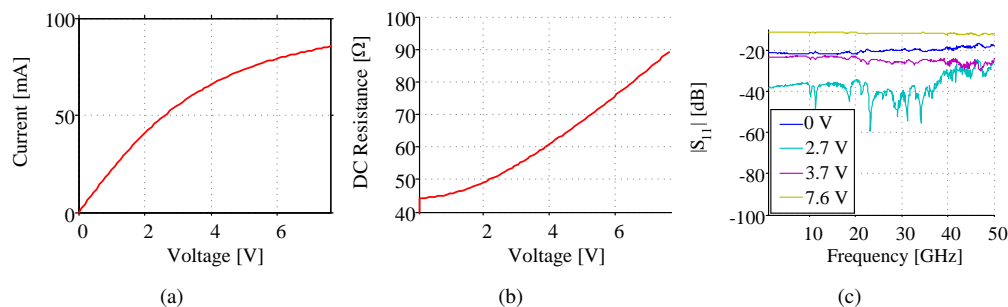

Fig. 13: Measurements of an on-chip termination designed to 50 Ω. In (a), the DC I-V measurement saturation effect is observed, and the calculated DC resistance is shown in (b). The small signal measurements at different DC voltages are shown in (c).

The S_{11} parameter, measured using a 50 GHz vector network analyzer (VNA), is shown in Fig. 13(c). The magnitude of the reflection when the DC resistance is 52 Ω (2.7 V bias) is very low over the entire 50 GHz band (S_{11} < -30 dB) indicating that these OCTs are broadband.

Even at 7.6 V, when the DC resistance is close to 90 Ω, the S_{11} magnitude is below -11.5 dB which is generally accepted as small.

3.4. *Small signal characterization*

Small signal characterization was performed using a 50 GHz Agilent N5225A/N4373D lightwave component analyzer, and 40 GHz GSSG probes. The effect of the instrument, cables, and probes were removed by performing a short-open-load-through (SOLT) calibration.

The measured electrical-electrical (EE) S_{11} response is shown in Fig. 14(a) and the reflection magnitude remains below -10 dB over 50 GHz for all reverse bias voltages tested. EE S_{21}, normalized at 1.5 GHz, for different reverse bias voltages are shown in Fig. 14(b). The -6.4 dB point at 2 V reverse bias is 38 GHz. At 4 V reverse bias, the -3 dB point is 28 GHz and the -6.4 dB point is beyond 50 GHz.
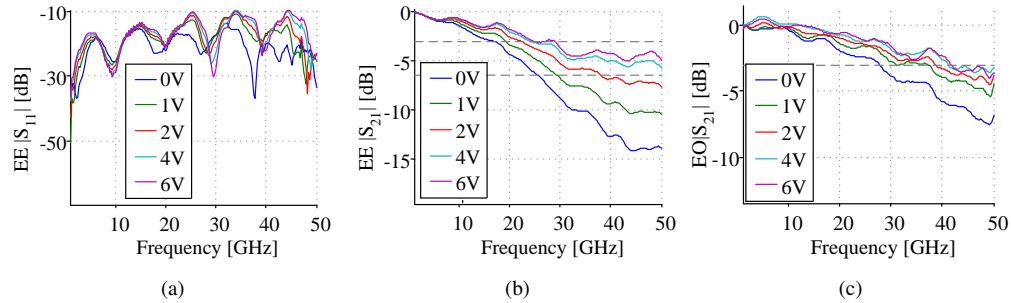

Fig. 14: S-parameter measurements: (a) EE S_{11}, (b) EE S_{21} normalized to 1.5 GHz (dashed lines mark -3 dB and -6.4 dB), and (c) EO S_{21} normalized to 1.5 GHz (dashed line marks -3 dB).

The measured EO S_{21} responses, normalized to 1.5 GHz, are shown in Fig. 14(c). Slight peaking is observed with increasing reverse bias, which is due the increase in impedance mismatch. At 1 V reverse bias, the response first approaches the -3 dB point at 33 GHz but only crosses -3 dB at 37 GHz. With 2 V and 4 V reverse bias, the -3 dB bandwidth increases to 38 GHz and 41 GHz, respectively. At 4 V, the response remains near the -3 dB line up to 50 GHz. This plateau in the S_{21} response at the -3 dB line has been observed in the measurements of several dies. The response also remains near the -3 dB line beyond 50 GHz. At 50 GHz, the EO response is only -3.2 dB. With an average $V_\pi L_\pi$ of 3.2 V-cm at 4 V bias estimated from Fig. 10(a) and Fig. 10(b), the RF V_π at 50 GHz is estimated to be 11.4 V.

The measured S-parameters with off-chip termination and on-chip termination are shown in Fig. 15. The reflection and transmission responses are almost identical despite the deviation in DC resistance from 50 Ω at 4 V for the OCT. This is because the bias voltage, in a SPP TWMZM, does not drop on the termination resistance and therefore the OCT's resistance remains close to 50 Ω. This comparison has not been made previously in this fabrication process, and demonstrates that using an OCT with a SPP modulator has no impairments on the small-signal frequency response.

In order to verify the attenuation, index and impedance mismatch, these parameters were extracted from measured EE S-parameters and are plotted in Fig. 16. The unloaded portion of the transmission line were de-embedded using simulations from HFSS. Unfortunately, the ripples in the measured S-parameters, originating from the impedance mismatch which creates a microwave free-spectral range, allowed only for sub-optimal extractions. Cleaner extractions can be obtained with a design that has a better impedance match. The attenuation follows a quadratic dependency with frequency, thus experimentally validating the prediction of Eq. (11).
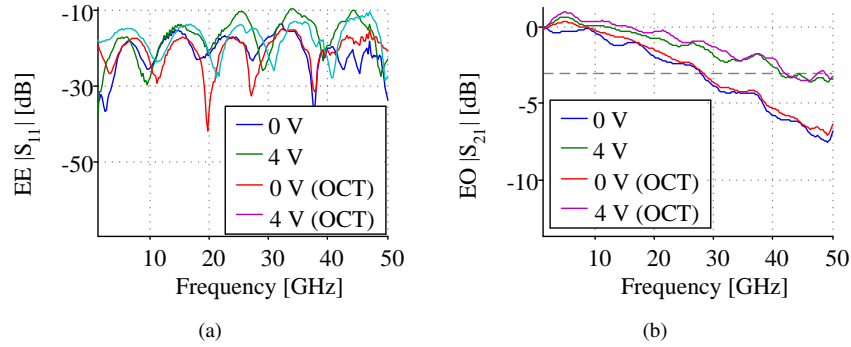
Fig. 15: S-parameter measurements with and without the on-chip termination: (a) EE S_{11}, and (b) EO S_{21} normalized to 1.5 GHz (solid line indicates -3 dB).

The frequency at 1.6 dB/mm (6.4 dB/4 mm) from the extracted attenuation is close to the measured EE -6.4 dB bandwidth. With a quadratic fit, the 1.6 dB/mm line is crossed at 44 GHz for 4 V reverse bias. The microwave index for 0 V at 30 GHz is 3.7, which is close to the simulated optical group index of 3.89 of the rib waveguide. At 4 V bias, the microwave index drops to 3.4 because of the reduced capacitance leading to a faster microwave propagation and the resulting index mismatch is 13%. A better match would result in the 3 dB EO bandwidth being closer to the 6.4 dB EE bandwidth, which is at least 50 GHz (the maximum measurable by our LCA) at 4 V bias as shown in Fig. 14. The characteristic impedance is close to 50 Ω at lower frequencies but increases for higher frequencies. These plots further indicate that the EE response is mainly limited by attenuation and that the residual index mismatch slightly lowers the theoretically attainable EO bandwidth.
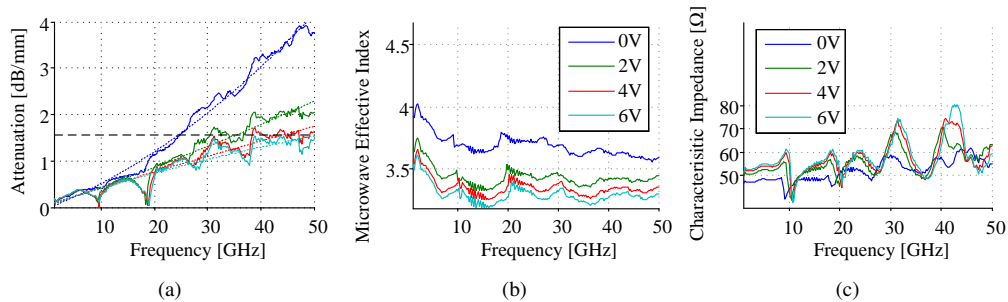

Fig. 16: Extracted (a) attenuation (quadratic fit shown by dashed line), (b) microwave phase index, and (c) characteristic impedance from measured RF S-parameters.

3.5. Large signal characterization: OOK modulation

The large signal behavior of the modulator was studied as part of a typical back-to-back bit-error-rate (BER) test link using a 56 Gbps SHF bit pattern generator (BPG), a 50 GHz SHF RF amplifier, a 35 GHz Picometrix photoreceiver, and an error detector. The optical eye diagrams at different bitrates with a PRBS-31 signal and a modulator driving voltage of 4.8 V_{pp} are shown in Fig. 17. Eyes with a clear opening are observed up to 60 Gbps. The extinction ratio (ER) and the Q-factor, measured with a digital communications analyzer (DCA) and an optical sampling module, are listed in the sub-caption. For all measurements, the modulator was set at quadrature

point. It is important to note that an EDFA, which limits the ER, had to be used to reach the sensitivity of the DCA. Furthermore, we report the ER and the Q-factor at quadrature with crossing points approximately at 50% and equal variance in one and zero levels. Higher ER and Q-factor can be obtained at the expense of larger modulation loss by biasing the modulator off-quadrature and squishing the zero-level.

(a) ER: 4.2 dB, Q:7.7   (b) ER: 3.9 dB, Q:3.9   (c) ER: 3.8 dB, Q:3.4
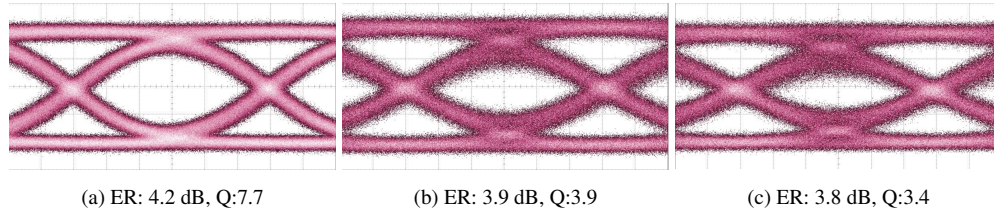
Fig. 17: Optical eye-diagrams with ER (in dB) and Q-factor (in linear units) measured with the DCA at (a) 40 Gbps, (b) 56 Gbps, and (c) 60 Gbps.

The change in ER for different driving and biasing voltages is shown in Fig. 18(a). At low bitrates, the ER improves by 2.5 dB for a drive voltage increasing from 4.8 V_{pp} to 8.1 V_{pp} (an increase in modulator power consumption by 2.8×). The ER decreases for higher reverse bias voltage because the phase shift achieved for the same drive voltage decreases with increasing bias as depicted by Fig. 11(a).

The sensitivity curves for 40 Gbps is shown for different reverse bias voltages with a drive voltage of 4.8 V_{pp} in Fig. 18(b). The 0 error line indicates an error-free measurement (BER $< 1 \times 10^{-12}$) with a 95% confidence level and also indicates that the receiver does not saturate in the tested range of received power. At 40 Gbps, error-free operation occurs with a received power of -6 dBm for a reverse bias of 6 V. The best sensitivity was observed for reverse bias voltages larger than -3 V. The performance is worst for 0 V bias, or for the case of as the diodes are not fully reverse-biased at this drive voltage. In a SPP configuration, only one diode conducts when the bias is left floating. In this case, a high ER and clean eyes were observed, however error-free operation could not be measured. The link was also observed to operate error-free up to 45 Gbps with a received power of 2 dBm (graph not shown).
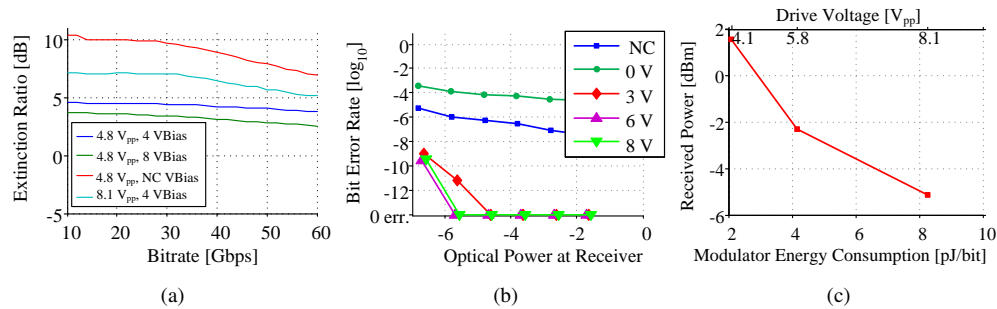

(a)   (b)   (c)

Fig. 18: Effect of drive and bias voltages for extinction ratio and receiver sensitivity. (a) Extinction ratio for different drive and bias voltages. (b) BER measurement for received power at different bias voltages at a drive voltage of 4.8 V_{pp} at 40 Gbps (NC: floating bias voltage). (c) Modulator energy consumption for error-free operation at 40 Gbps and the required optical power at receiver (modulator biased at 4 V).

As is known, modulators can be operated with drive voltages lower than that required for a π phase shift. A larger driving voltage, however, reduces the optical power necessary at the

receiver illustrating a trade-off between laser and modulator power consumption. Figure 18(c) quantifies this by plotting the measured optical power at the receiver for error-free operation at 40 Gbps and the corresponding drive voltage and energy consumed by the SPP TWMZM.

3.6.   Large signal characterization: OOK modulation with analog signal processing (ASP)

Higher bitrate operation can be achieved using pre-emphasized signals, which can be formed with passive analog components. Such continuous time filtering techniques have also been implemented on chip for electronic dispersion compensation in transceivers. This has been previously employed with forward bias modulators [28, 29] to overcome the bandwidth limitation of the modulator. Here it is repeated for reverse bias operation to overcome the limitation of the BPG. The two-tap feed-forward equalizer (FFE) illustrated in Fig. 19(a) was applied using analog components and its calculated response is shown in Fig. 19(b). In the experiment, the delay was introduced with discrete tunable delay lines, the coefficients of the filter were set by changing the drive voltages of two synchronized channels of the BPG, and the outputs were summed using a passive power combiner. This filter principally compensates for the frequency response of the BPG, whose bandwidth is estimated to 28 GHz from rise time measurements. The resulting driving signal had a voltage of 6.21 V_{pp} and 1.74 V_{rms}.

$\{h[0] = 1, h[1] = -0.62, \tau = 3.2 \text{ ps}\}$

$T(f) = 1 - 0.62e^{-i2\pi f(3.16 \times 10^{-12})}$

(a)   (b)
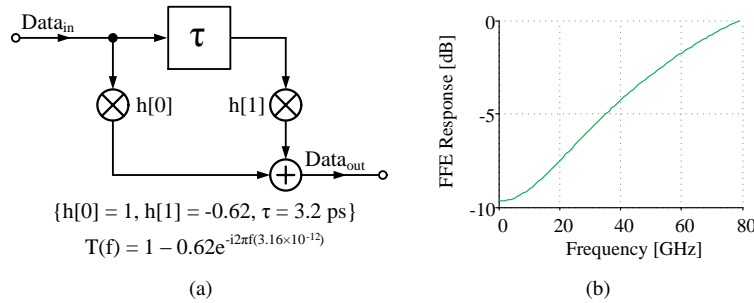
Fig. 19: (a) Two-tap passive FFE and (b) Calculated response of the two-tap FFE.

The optical eye diagrams at different bitrates with a PRBS-31 signal are shown in Fig. 20. Comparing the eyes at 60 Gbps of Fig. 20(a) and Fig. 17(c), the eye with ASP has very little ISI. The signal, however, is noisier. With this passive filtering approach, clear openings are seen up to 70 Gbps. The extinction ratio at 60 Gbps is 2.1 dB greater than observed in Fig. 17 and the Q-factor is also slightly better. The eye diagrams are noisier due to the attenuation by the equalizer used to compensate the BPG. Even at 72 Gbps, where the zero and one levels of the eye diagram still have a flat level indicating that the performance at these bitrates is not limited by bandwidth. In fact, Fig. 20(a) shows about 5.6 ps of flat levels, corresponding to an eye period of 11.1 ps and 90 Gbps.

Even at 72 Gbps, the zero and one levels of the eye diagram have a flat level indicating that the performance at that bitrate is now limited by noise and not by bandwidth. With this experiment, it can be inferred that with a faster BPG, our TWMZM will operate at bitrates beyond the 60 Gbps measured in section 3.5.

The limitation of using only two-taps for the pre-emphasis filters is that the low-frequency content is cut-off, which can lead to baseline wander and pattern dependent errors [28]. Furthermore, with the limited taps, it is not possible to design a filter that would optimize for both noise and bandwidth. These issues can be mitigated with digital signal processing.

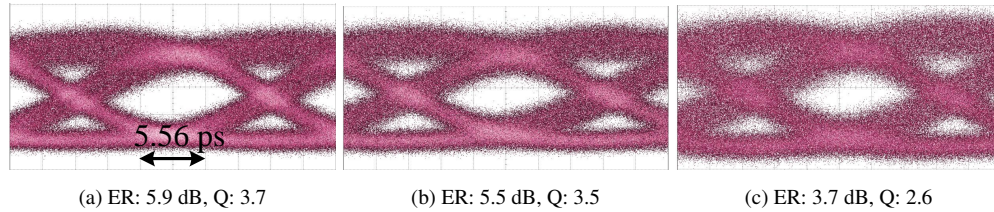| (a) ER: 5.9 dB, Q: 3.7 | (b) ER: 5.5 dB, Q: 3.5 | (c) ER: 3.7 dB, Q: 2.6 |

Fig. 20: Optical eye-diagrams with ER (in dB) and Q-factor (in linear units) measured with the DCA and with analog pre-emphasis at (a) 60 Gbps, (b) 70 Gbps, and (c) 72 Gbps.

3.7. Large signal characterization: OOK and PAM modulation with DSP

This section presents the testing of the silicon modulator using DSP with slight modifications from the method employed in [12, 13, 30]. In contrast to [12] and [13], this experiment is performed in the C-band and using a TWMZM that has almost twice the EO bandwidth with a larger V_π. A schematic of the experimental setup is shown in Fig. 21.
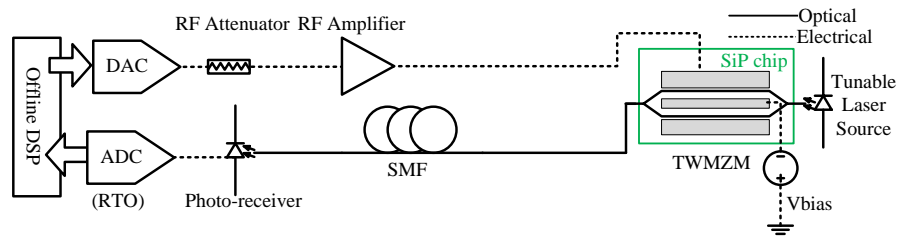

Fig. 21: DSP communication link.

The data to be transmitted was generated using offline DSP and then uploaded to a 70 GSamples/s (GSPS) 8-bit digital-to-analog converter (DAC). For the PAM-8 format, which requires greater linearity, an attenuator was placed to avoid gain compression from the amplifier. On the optical side, a tunable laser source was used to bias the modulator at quadrature. The modulated signal was launched into different fiber lengths of Corning SMF-28e+ fiber. On the receiver side, a differential-out 35 GHz Picometrix photoreceiver was used to convert light to the electrical domain. The differential cables were skew-matched and connected to the ADC. A real-time oscilloscope (RTO) with a 33 GHz bandwidth, 8-bit resolution, and a sampling rate of 80 GSPS was used as the analog-to-digital (ADC) converter.

The sequential steps of the transmitter offline DSP, depicted in Fig. 22, is discussed next. Instead of generating a binary pattern and then applying a Gray-coding, the symbols themselves were randomly generated as integers equally spaced apart and spanning the PAM order. This pseudo-random integer sequence (PRIS) pattern was up-sampled to the DAC sampling rate by inserting ($\frac{70}{B} - 1$) zeros, where B is the baudrate in GBaud. Afterwards, a raised-root cosine (RRC) pulse-shaping filter $G(f)$ with a roll-off factor parameter $\alpha \in [0,1]$ was applied. This filter interpolates the data to the DAC's sampling rate and also limits the bandwidth of the data stream to $\frac{1}{2}B(1+\alpha)$. With a larger roll-off factor, a higher bandwidth is required but a wider ISI-free sampling window can be obtained. The pulse shaped data was passed through an inverse sine filter to compensate for the non-linearity of the MZM sinusoidal transfer function. A pre-emphasis filter $H(f)$, obtained from a least-mean-squares (LMS) algorithm using a training sequence, was then applied to compensate for the limitations of the entire system. The processed signal was then quantized to 8-bit and uploaded to the DAC's memory for transmis-
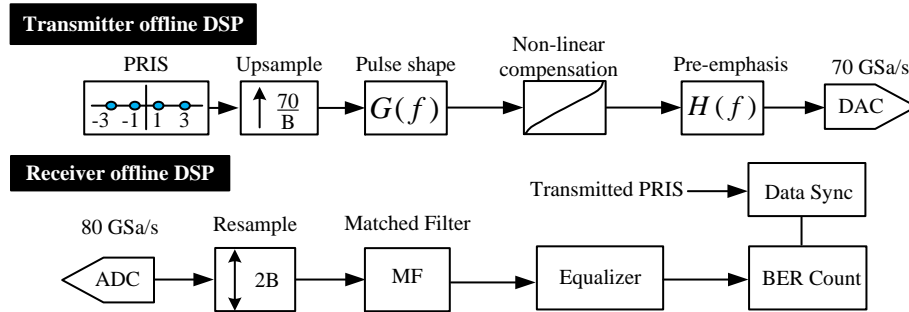
sion.

Fig. 22: Transmitter and receiver offline DSP.

On the receiver side, the data captured by the ADC at 80 GSPS was re-sampled to twice the symbol rate $2 \times B$. Then, a RRC matched filter was applied to the data. Afterwards, the data was equalized with a finite-impulse-response (FIR) filter, whose coefficients were also obtained from a training sequence. After equalization, the BER was obtained by decoding the multi-level received and transmitted patterns into a binary stream and then comparing the bits. In the testing setup used for this experiment, the DAC and ADC clocks were synchronized and no digital clock recovery was required. Clock recovery can be performed with DSP, if necessary, as described in [13].

The bandwidth of the transmit-receive chain (excluding the ADC) is estimated to be 8 GHz and is mainly limited by the DAC's bandwidth (specified as >13 GHz). This indicates that for a communication link with DSP and error correction coding, low error rate transmission at high bitrates can be obtained with low bandwidth MZMs.

The spectrum of the root-raised cosine pulse-shaped data is shown in Fig. 23(a). In Fig. 23(b), the pre-emphasis filters ($H(f)$ of Fig. 22) that were applied at the transmitter for OOK (PAM-2), PAM-4, and PAM-8 are shown. For each modulation format, the filters were optimized for transmission at different baudrates and a fixed distance of 2 km. For PAM-2, PAM-4, and PAM-8, the baudrate used for optimization were 70, 56, and 37, respectively. The optimum roll-off factor of PAM-2, PAM-4, and PAM-8, were 0.9, 0.1, and 0.4, respectively. For PAM-2, the frequency content from 20 to 35 GHz is emphasized and the lower frequency content remained near -10 dB. For PAM-8, compensation was done from -11 dB near DC up to about 28 GHz. For PAM-8, the pre-emphasis filter was the inverse of the DAC response up to 25 GHz. For PAM-4, the emphasis is similar to PAM-8, except that the lower frequency components are not attenuated as much. Since the LMS algorithm was used to obtain these filters, the pre-emphasis filters do not simply compensate for bandwidth and are not the inverse of the analog response of the components. The quick roll-off of the PAM-4 and PAM-8 filters is mainly due to the sharp cut-off of the spectrum of the pulse-shaped transmitted data.
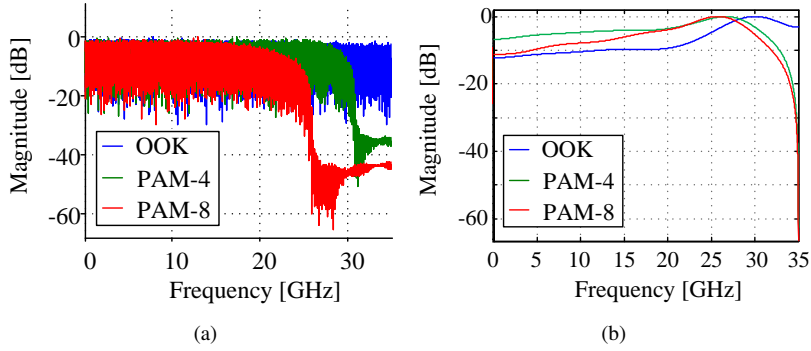
Fig. 23: Frequency spectrum of (a) root-raised cosine pulse shaped data at the transmitter, and (b) the pre-emphasis filters applied at the transmitter for OOK, PAM-4, and PAM-8 modulation formats.
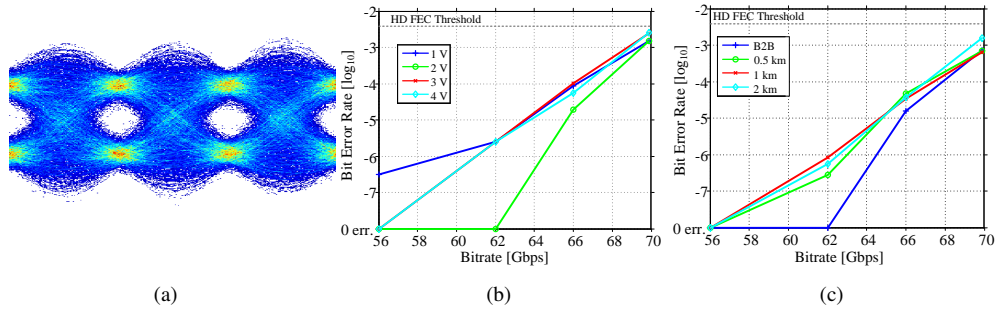
3.7.1. PAM-2 modulation

Fig. 24: PAM-2 modulation results with DSP. Shown in (a) is the eye diagram, (b) BER for different bias voltages, and (c) BER for different transmission distances at 2 V reverse bias.

The results for OOK modulation with DSP are shown in Fig. 24. In Fig. 24(b), the BER after 2 km of propagation for different reverse bias voltage of the modulator and transmission speeds is plotted. The best performance was observed for a reverse-bias voltage of 2 V and the experiment was repeated for different fiber lengths at that bias voltage. A slight degradation in BER is observed for the 2 km distance compared to the shorter distances. This is believed to be due to the chromatic dispersion present at 1550 nm.

According to the ITU-T G.709 standard, a 6.7% overhead is allotted for forward error correction (FEC) coding. With a pre-FEC hard-decision (HD) BER threshold of 3.8×10^{-3}, a corrected BER of 1×10^{-15} (considered error-free) can be obtained with a coding scheme that has a net coding gain of 9.2 dB. Such gains are achievable by super-FEC (or enhanced-FEC) codes, and this BER threshold is generally accepted to be error-free for long-haul transmission.

Without FEC, the BER at 70 Gbps for 2 km of propagation is 1.57×10^{-3}. Thus, with FEC and framing overhead, this can be considered error-free at 62 Gbps.

The measured drive voltage for OOK with DSP was 4.3 V_{pp} and 0.98 V_{rms}.

3.7.2. PAM-4 modulation

The results for PAM-4 modulation with DSP are shown in Fig. 25. In Fig. 25(b), the BER after 2 km of propagation for different reverse bias voltage of the modulator and transmission speeds
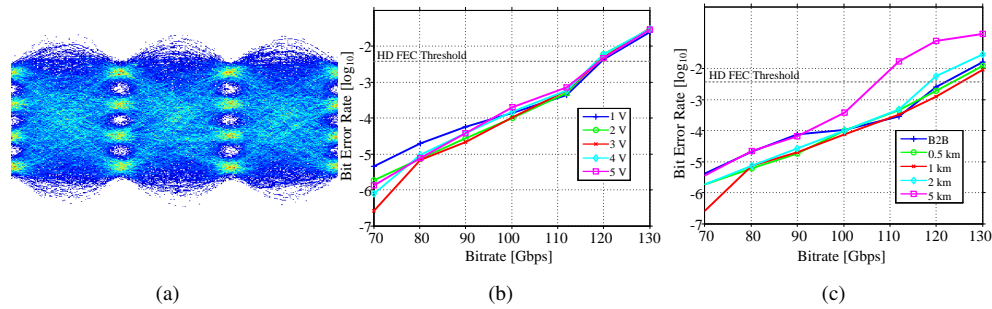
Fig. 25: PAM-4 modulation results with DSP. Shown in (a) is the eye diagram, (b) BER for different bias voltages, and (c) BER for different transmission distances at 2 V reverse bias.

is plotted. At 112 Gbps, the best performance was observed for a reverse-bias voltage of 2 V. At that bias voltage, the experiment was repeated for different fiber lengths.

Without FEC, the BER at 112 Gbps for 2 km of propagation is 4.92×10^{-4}. Thus, with FEC and framing overhead, this can be considered error-free at 100 Gbps.

The measured drive voltage for PAM-4 with DSP was 5.21 V_{pp} and 0.94 V_{rms}.
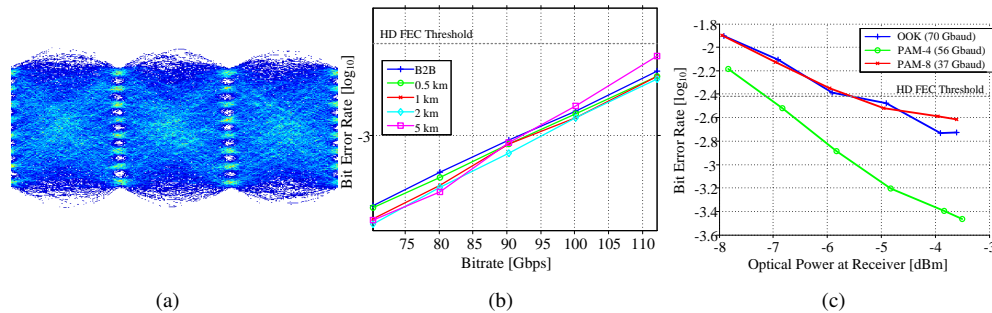
3.7.3. PAM-8 modulation

Fig. 26: PAM-8 modulation results with DSP. Shown in (a) is the eye diagram, (b) BER for different transmission distances at 1 V reverse bias, and (c) the sensitivity of the receiver for the different modulation formats after 2 km of propagation.

In Fig. 26(b), the BER after propagation for different fiber lengths at a reverse bias voltage of -1 V is shown. Without FEC, the BER at 112 Gbps for 5 km of propagation is 3.16×10^{-3}. Thus, with FEC and framing overhead, this can be considered error-free at 100 Gbps. PAM-8 operation was observed to operate below FEC threshold for 5 km of fiber as opposed to 2 km of fiber with PAM-4. This is most likely due to the larger roll-off factor used with the PAM-8 modulation format making it more tolerant to ISI from pulse broadening. Furthermore, the RMS drive voltage for PAM-8 modulation format was also higher than for the PAM-4 case.

The measured drive voltage for PAM-8 with DSP was 6.73 V_{pp} and 1.32 V_{rms}.

In Fig. 26(c), the receiver sensitivity after 2 km of propagation for the three cases are compared. It is observed that for PAM-8, the BER falls below the FEC threshold for received optical power greater than -5.4 dBm. The optical power requirement for PAM-4 is lower, it is below FEC threshold for received powers larger than -7.1 dBm.

3.8. Modulator energy estimate

A disadvantage of the SPP modulator is the higher drive voltage required from a single modulator driver. In a dual-drive modulator the voltage is shared among two drivers and this results in a dynamic power consumption that is almost half of the SPP TWMZM (assuming linear phase shift with voltage). However, in a SPP, the bias voltage does not drop across the termination resistance and the static power consumed is negligible.

For DSP, the drive voltage is sensitive to the roll-off factor and the clipping ratio applied at the transmitter side. A simple approach to estimate the power consumption is to use the RMS voltage and assume that power is mainly consumed by the termination resistor. Then, the dynamic power can be estimated as $P_{Dynamic} = V_{rms}^2/R_T$, where R_T is the termination impedance. It is implied that the transmission line is impedance matched to the source and termination as is commonly assumed in energy reports of TWMZMs [20, 31, 32].

The power consumed by the modulator for each driving configuration is listed in Table 1. For the case without signal processing, the bitrate used is 40 Gbps and the driving voltage corresponds to error-free transmission with a received power of -5.17 dBm. The DSP cases used are also considered error-free post-FEC. Error counting could not be performed for the case with ASP due to the lack of a fast photoreceiver, a bitrate of 60 Gbps is assumed. The bitrates used in the energy estimation for the cases with FEC is the approximate bitrate of the payload.

Table 1: Estimated power consumed by the SPP TWMZM for different modulation configurations.

Modulation Format	Bitrate [Gbps]	V_{rms}	$P_{Dynamic}$ [W]	Energy [pJ/bit]
OOK	40	4.07	0.33	8.27
OOK (ASP)	60	1.74	0.06	0.96
OOK (DSP)	62	0.98	0.019	0.31
PAM 4 (DSP)	100	0.94	0.018	0.18
PAM8 (DSP)	100	1.32	0.035	0.35

These calculations show that with signal processing the power consumed by the TWMZM is reduced. The energy per bit of the TWMZM is also lower with signal processing because of the higher bitrate. The lowest energy consumption is for PAM-4. PAM-8 had twice the power consumption. This table illustrates how the power consumption is transferred from the modulator to the analog (power consumed by the passive combiner) and digital (DAC, coders, decoders, ADCs, etc.) components. Although DSP increases power consumption, it has been actively considered by the IEEE 802.3bs taskforce for 400 Gbps ethernet [33].

4. Conclusion

The design and analysis of a SPP TWMZM is presented. The modulator is developed with the goal of optimizing the electro-optic bandwidth. As such, a SPP structure is used to reduce microwave loss and a slow-wave electrode is used to increase the microwave index. The characteristic impedance target of 50 Ω, for matching with commonly available microwave drivers and terminations, is achieved at lower frequencies and small bias voltages.

At a reverse-bias voltage of 4 V, the -3 dB electro-optic bandwidth is measured to be 41 GHz, to the best of our knowledge, this is the highest reported bandwidth for a SiP modulator with 4 mm of p-n junction loading. Due to variations in fabrication, the DC V_π is different for both arms of the MZM. The average $V_\pi L_\pi$ estimated from phase shift measurements at 4 V bias is 3.2 V-cm. At 4 V bias, the RF V_π at 50 GHz is estimated to be 11.4 V.

For on-off keying modulation, open eye diagrams are visible up to 60 Gbps. Error-free operation with a BER $< 1\times10^{-12}$ is measured up to 45 Gbps, the limit of our photoreceiver. The bandwidth of the BPG was compensated with a passive filter and eye diagrams with a clear opening up to 70 Gbps are observed. The device was further characterized using DSP to compensate for the analog bandwidth limitations of the entire communication link. Using PAM-4, 112 Gbps transmission on 2 km of SMF fiber is achieved below the pre-FEC BER threshold of 3.8×10^{-3}. This corresponds to error-free (BER of 1×10^{-15}) 100 Gbps operation given a net coding gain of 9.2 dB. With the PAM-8 modulation format, this is accomplished up to a distance of 5 km. Energy consumed by only the modulator for the different driving configurations of our experiment were calculated and the lowest energy consumed by the modulator is found to be for PAM-4 with 0.18 pJ/bit.

This work demonstrate the ability to create high bandwidth modulators in the silicon photonic technology. Using DSP, 100 Gbps modulation using a single wavelength intensity modulation was shown, which can be an alternative to coherent-based high-speed on-chip transceivers [34]. The device also has applications in supercomputers and data centers [35], as well as passive and active optical interconnects [36]. Using multiplexing and the experiment presented in this paper, 400 Gbps and 1 Tbps silicon photonic short reach optical interconnects can be developed.